Title: Modelling, manufacturability and compression properties of the CpTi grade 2 cellular lattice with radial gradient TPMS architecture

Author: Joanna Maszybrocka, Bartosz Gapiński, Michał Dworak, Grzegorz Skrabalak, Andrzej Stwora

Citation style: Maszybrocka Joanna, Gapiński Bartosz, Dworak Michał, Skrabalak Grzegorz, Stwora Andrzej. (2019). Modelling, manufacturability and compression properties of the CpTi grade 2 cellular lattice with radial gradient TPMS architecture. "Bulletin of the Polish Academy of Sciences Technical Sciences" (2019, nr 4, s. 719-727), DOI: 10.24425/bpasts.2019.130181

BULLETIN OF THE POLISH ACADEMY OF SCIENCES
TECHNICAL SCIENCES, Vol. 67, No. 4, 2019
DOI: 10.24425/bpasts.2019.130181

Modelling, manufacturability and compression properties of the CpTi grade 2 cellular lattice with radial gradient TPMS architecture

J. MASZYBROCKA[1]*, B. GAPIŃSKI[2], M. DWORAK[1], G. SKRABALAK[3], and A. STWORA[3]

[1] University of Silesia, Institute of Materials Science, 75 Pułku Piechoty 1A, 41-500 Chorzów
[2] Poznań University of Technology, Institute of Mechanical Technology, Piotrowo 3, 60-965 Poznań
[3] Institute of Advanced Manufacturing Technology, Wrocławska 37A, 30-011 Krakow

Abstract. In the present study, a titanium cellular lattice structure with a mathematical designed porosity gradient was successfully fabricated using the selective laser melting method. The samples with smooth gradient transition of porosity of between 60% and 80% were received for different elementary cell geometries. Elementary cells belong to the triply periodic minimal surfaces family (G, D, I2Y, IWP). Each sample was subjected to a comprehensive analysis including: dimensional metrology and assessment of material defects (X-ray micro-tomography), surface morphology tests (scanning electron microscopy) and mechanical properties (universal testing machine). It has been shown that a cellular lattice with high dimensional accuracy (+0.16/–0.08 mm) and full dense struts can be obtained. According to the assumption, the gradient increases the strength of the cellular lattice samples. The highest increase in plateau stress between the samples with and without gradient was found for the I2Y series (about 185%). Furthermore, it was found that the stress-strain response of the samples depends not only on total porosity, but also on the 3D geometry of the cellular lattice. The stress-strain curves for G, IWP and I2Y samples are smooth and exhibit three characteristic regions: linear elasticity, plateau region and densification region. The size of regions depends on the geometric features of the cellular lattice. For series D, in the plateau region, the fluctuations in stress value are clearly visible. The smoothest stress-strain curve can be noted for the G series, which combined with good mechanical properties (the plateau stress and energy absorbed, at respectively 25.5 and 43.2 MPa, and 46.3J and 59.5J for Gyr_80 and Gyr_6080, which corresponds to a strain of almost 65% and 50%) positively affects the applicability of cellular structures with such geometry.

Key words: selective laser sintering, additive manufacturing, cellular lattice, triply periodic minimal surfaces, mechanical properties.

1. Introduction

The specific spatial structure of materials with cellular structure implies their unique properties, thanks to which they have been widely used for many years, among others as elements of car catalysts, heat exchangers, crumple zones in vehicles or ballistic panels [1–4].

Highly porous titanium and titanium alloys play an important role as bone implants, as evidenced by *in vitro* and *in vivo* studies [5–7]. The use of implants with porous structure helps avoid inadequate straining of the underlying bone tissue and reduce the problem of stress shielding associated with solid implants [8–10]. It is assumed that optimum pore size should be in the range of 100–700 μm. The pores should be open and the degree of porosity should stand at 60–80% [11–13]. Unfortunately, an increase in the implant's porosity degrades its mechanical properties. A solution to this problem could in the form of porous structures with a porosity gradient. A compromise between the required porosity and appropriate mechanical properties can be obtained in samples with a highly porous outer shell and a solid or less porous core.

To date, many traditional fabrication processes, such as powder metallurgy with space holder, compression and fiber sintering, sponge replication and the freeze-casting method, were reported to fabricate porous structures [1, 2, 7]. Unfortunately, none of these methods allows to obtain samples with precisely defined porosity, pore shape, size and interconnectivity. Thus the above-mentioned methods do not allow to build components with a porosity gradient either.

Among the technologies for the production of cellular metallic materials, additive manufacturing methods are becoming increasingly prominent. One of the fabrication methods for powder components is the selective laser sintering / melting technology (SLS/SLM). During the process, the laser beam, layer by layer, sinters metallic powders according to the previously prepared geometries / toolpaths describing the individual cross-sections of the object being created [14, 15]. This technology makes it possible to create complex 3-D freeform objects directly from a computer model.

The mechanical properties of cellular materials depend on the material and topology of their skeleton. The key stage is the preparation of a spatial model of the structure to be produced. There are many approaches to cellular lattice design. Usually, an elementary cell model is developed in CAD software with the help of basic objects (e.g. sphere, cylinder, cube) and logical operations. Then it is replicated in space. Many scaffold libraries were developed in this manner, and their basic mechanical properties were described [16–18].

Recently, a generation of scaffolds using triply periodic minimal surfaces (TPMS) has been developed. TPMS are smooth infinite surfaces that partition space into two intertwined lab-

*e-mail: joanna.maszybrocka@us.edu.pl

Manuscript submitted 2018-11-14, revised 2019-01-18, initially accepted for publication 2019-02-13, published in August 2019

yrinthine domains [19–21]. The selection of the appropriate function and its parameters enabled controlled change of the shape, size and distribution of pores, and also allowed to control the total porosity of the model.

The advantages of using the TPMS structure from the Ti6Al4V alloy have been previously reported in the literature. Interdisciplinary studies include the evaluation of their surface topography, dimensional accuracy or mechanical properties [22, 23]. A few number of studies concern cellular lattices from Cp-Ti grade 2 [24], especially in relation to structures with a porosity gradient.

The aim of this work is to model cellular lattice structures based on selected TPMS architectures that will have a precisely designed porosity gradient, and then to evaluate their manufacturability by means of selective laser melting and investigate their mechanical properties in a uniaxial compression test.

2. Materials and methods

2.1. TPMS mesh surface generation. For modelling purposes, four types of TPMS were selected (Fig. 1). Selected TPMS were approximated with periodic surfaces composed of simple trigonometric functions:

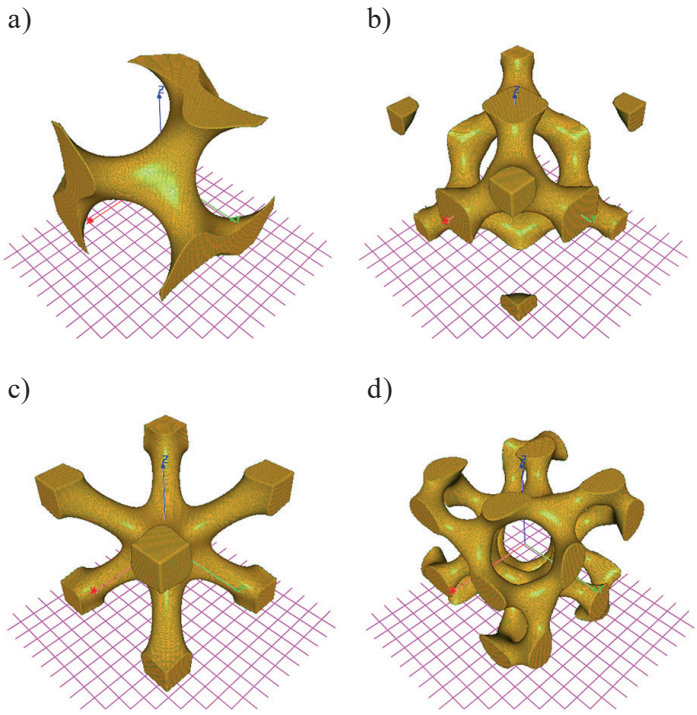

Fig. 1. Basic unit cell: a) Gyr, b) Diam, c) IWP, d) I2Y

$$\Phi_G(x,y,z) = k_1\cdot\big(\cos(x)\cdot\sin(y)+\cos(y)\cdot\sin(z)+\cos(z)\cdot\sin(x)\big) - k_2\cdot\big(\cos(2\cdot x)\cdot\cos(2\cdot y)+ + \cos(2\cdot z)\cdot\cos(2\cdot x)\big) - k_3 \tag{1}$$

$$\Phi_D(x,y,z) = k_1\cdot\big(\sin(x)\cdot\sin(y)\cdot\sin(z)+\sin(x)\cdot\cos(y)\cdot\cos(z)+\cos(x)\cdot\sin(y)\cdot\cos(z)+ \cos(x)\cdot\cos(y)\cdot\sin(z)\big) - k_2\cdot\big(\cos(4\cdot x)+\cos(4\cdot y)+\cos(4\cdot z)\big) - k_3 \tag{2}$$

$$\Phi_{IWP}(x,y,z) = k_1\cdot\big(\cos(x)\cdot\cos(y)+\cos(y)\cdot\cos(z)+\cos(z)\cos(x)\big) - k_2\cdot\big(\cos(2\cdot x)+ - k_2\cdot\big(\cos(2\cdot x)+\cos(2\cdot y)+\cos(2\cdot z)\big) - k_3 \tag{3}$$

$$\Phi_{I2Y}(x,y,z) = -k_1\cdot\big(\sin(2\cdot x)\cdot\cos(y)\cdot\sin(z)+\sin(2\cdot y)\cdot\cos(z)\cdot\sin(x)+\sin(2\cdot z)\cdot\cos(x)\cdot\sin(y)\big) - - k_2\cdot\big(\cos(2\cdot x)\cdot\cos(2\cdot y)+\cos(2\cdot y)\cdot\cos(2\cdot z)+\cos(2\cdot z)\cdot\cos(2\cdot x)\big) - k_3 \tag{4}$$

The model parameters (k_1, k_2, k_3) for each type of TPMS were chosen to prepare two variants of the structure, with porosity $V_v = 80\%$ and $V_v = 60\%$. The volume ratio V_v was defined as the ratio of the volume of pores to the total volume of the surrounding area of the model.

$$V_v = \frac{V_{pores}}{V_{tot}} \tag{5}$$

where:

V_{pores} – volume of pores
V_{tot} – total volume of the surrounding area.

It was assumed that the area of modelling will constitute a cylinder with diameter Ø15 mm and height of 15 mm. In order to obtain smooth transition between porosity $V_v = 60\%$ from the core of the sample up to 80% on the outer layer, the entire structure was described by one continuous function Φ_{GRAD}:

$$\Phi_{GRAD}(x,y,z) = \alpha(x,y,z)\cdot\Phi_{TPMS\_v1}(x,y,z) + + \big(1-\alpha(x,y,z)\cdot\Phi_{TPSM\_v2}(x,y,z)\big) \tag{6}$$

Φ_{TPMS_v1} and Φ_{TPMS_v1} indicate the type of the structure (described by equations 1–4), respectively, with porosity $V_1 = 60\%$ and $V_2 = 80\%$. The weight function $\alpha(x, y, z)$ is described by the following equation:

$$\alpha(x,y,z) = \frac{V_{pores}}{1+e^{-k\cdot G(x,y,z)}} \tag{7}$$

$G(x, y, z) = 0$ is the transition boundary between Φ_{TPMS_v1} and Φ_{TPMS_v1} and the constant k describes the transition gradient.

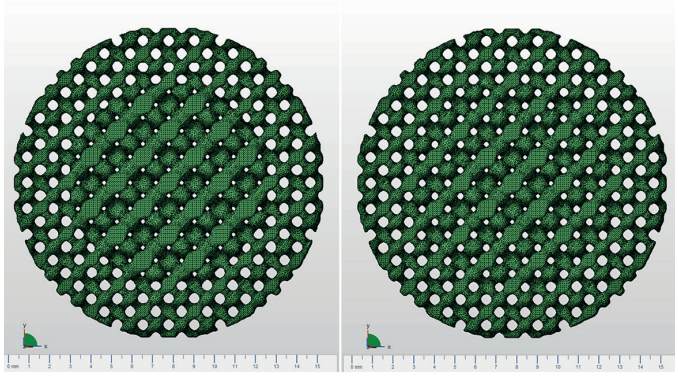

Fig. 2. Example of the model with gradient porosity and different transition boundary size

8 types of samples were prepared for further studies: four base models without gradient porosity (total porosity was 80%) and four models with smooth, radial gradient porosity varying from 60% to 80%. The three-dimensional mesh as a set of coordinates of the vertices and the set of elements that define the topology of the grid has been exported to an *.stl format. The finished models are shown in Fig. 3 and their basic parameters are presented in Table 1.

Table 1
Basic parameters of the cellular lattice model

Name	S [cm^2]	V [cm^3]	V_v [%]	S/V [cm^2/cm^3]
Diam_80	35.1	0.54	79.6	65.0
Gyr_80	28.2	0.51	80.8	55.3
IWP_80	32.2	0.54	79.6	59.6
I2Y_80	48.2	0.49	81.5	98.4
Diam_6080	36.2	0.63	76.2	57.5
Gyr_6080	29.5	0.62	76.6	47.6
IWP_6080	34.8	0.69	74.0	50.4
I2Y_6080	52.8	0.66	75.1	80.0

where: S – surface area, V – volume of the model,
V_v – total porosity of the model, S/V – surface area to volume ratio

2.2. Selective laser melting of the cellular lattice specimens. Cellular lattice specimens were made on the Renishaw AM250 selective laser melting (SLM) device from commercially available Cp-Ti grade 2 powder. The powder's chemical composition

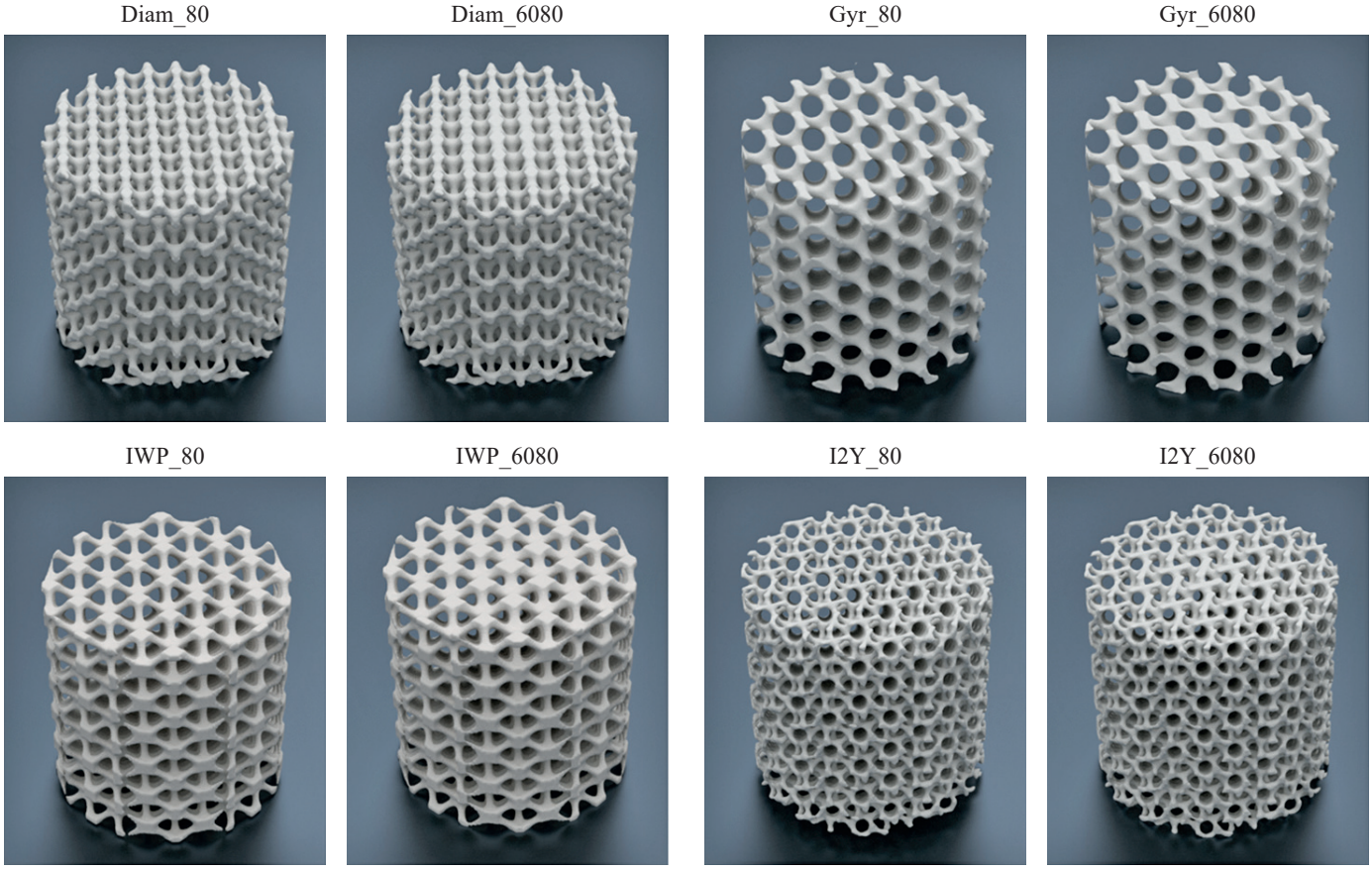

Fig. 3. Visualization of the cellular lattice model

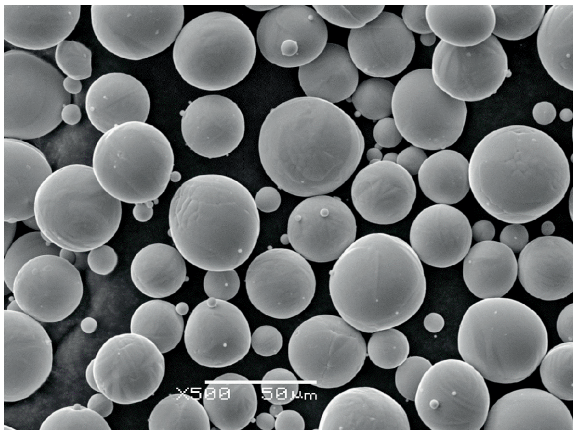

Fig. 4. Cp-Ti grade 2 powder (SEM)

corresponds to ASTM F67. Microphotographs of the powders are shown in Fig. 4. Their particles were almost spherical with smooth surface morphology. The powder particles diameter ranged from 5 to 45 µm in size.

The Renishaw AM250 selective laser melting machine was equipped with a modulated pulse laser with maximum power of 400 W and wavelength of 1064 nm. The SLM processes was performed in an inert atmosphere of argon, with the oxygen level limited to 500 ppm. The parameters of the sintering process are summarized in Table 2.

Table 2
Selective laser sintering parameters

Laser power	**Scan speed**	**Point distance**
300 W	300 mm/s	65 µm
Exposure time	**Layer thickness**	**Scan strategy**
65 ms	50 µm	meander

After the sintering process, the samples were cut from the base plate using wire electrical discharge machining (WEDM). In order to remove any trapped loose powder, the samples were cleaned with a flow of compressed air and then put through an ultrasonic cleaner.

2.3. SEM investigation. Microscopic observations of the samples were made on a JEOL JEM-3010 scanning microscope. Observations were carried out on an inclined table. This allowed to reflect the three-dimensional nature of the structure.

2.4. Tomographic studies. Inspection of geometrical features and porosity was carried out by means of computed tomography. This method is used increasingly often for this purpose [25, 26]. It is also applied when verification of workpieces manufactured by rapid additive techniques is concerned [27]. Tomographic studies were carried out on the measuring GE v|tome|x s 240 X-ray tomographic scanner with a reflection target tube. All the tests were performed using the same measuring strategy. The voxel size was 23.2 µm, and 1400 projections (every one of those takes 600 ms) were made. Power of the X-ray source was 28.5 W (150 kV and 190 µA). For reconstruction, GE Datos software with beam hardening effect correction was used. Qualitative and quantitative analysis of outer shape and inner structure was made in specialized Volume Graphics software.

2.5. Uniaxial compression test. Uniaxial compression tests were carried out using an Instron 5982 universal testing machine equipped with a 100 kN load cell, with constant crosshead speed of 0.3 mm/min. Tests were carried out in room temperature. During the measurement, compression stress versus compression strain data were recorded. The compression strain data were precisely recorded with an Instron 2663 video extensometer. Stress was computed from the load and cross-sectional area of the sample.

3. Results

3.1. Surface morphology. Scanning electron microscopy observations show that any loose powders that could remain inside the cellular lattice following the sintering process were effectively removed from the pores (Fig. 5, 6).

a)

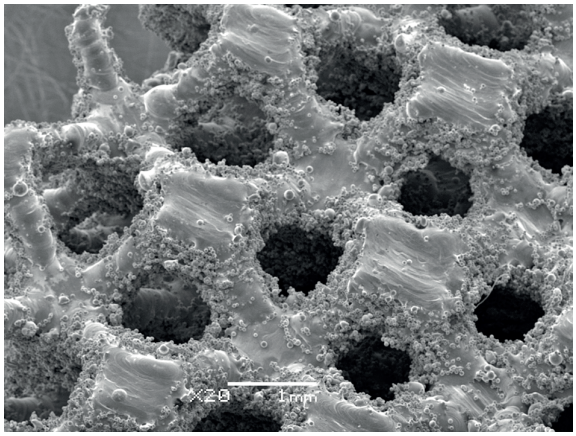

b)

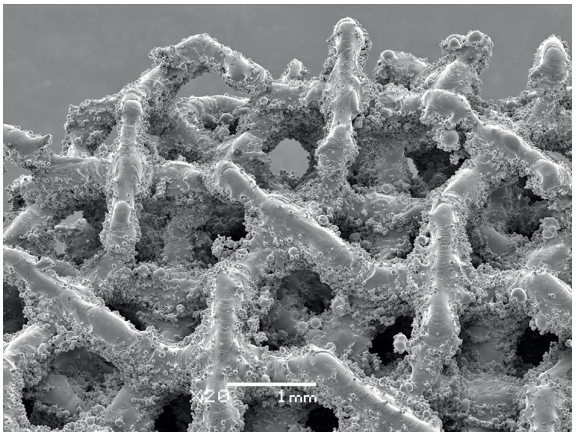

Fig. 5. Cellular lattice structures: a) Gyr_6080 b) Diam_6080, as manufactured by SLM (SEM)

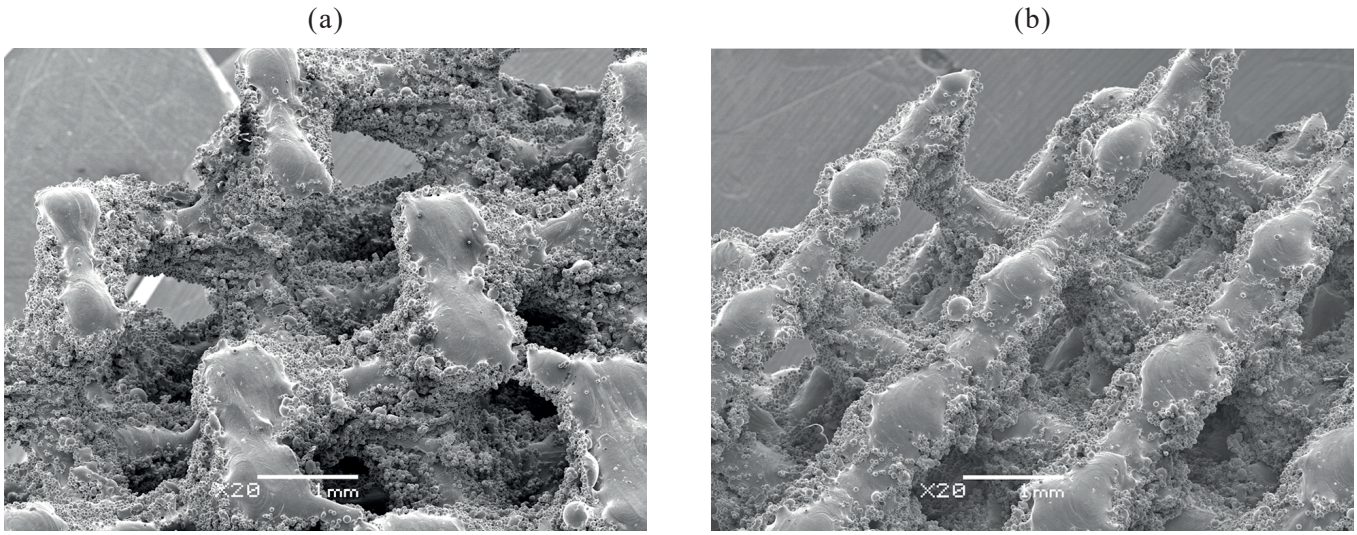

Fig. 6. Cellular lattice structures: a) IWP_6080 b) I2Y_6080, as manufactured by SLM (SEM)

However, massive amounts of partially melted powder have been attached to struts surfaces, which increases their surface roughness. This is particularly visible on the direction perpendicular to building direction and it is also characteristic for the struts with an inclined angle. The surface roughness in this case is determined by the laser penetration and infiltration effect [28]. Bearing in mind the mechanical properties, it should be emphasized that such irregular surfaces are not desirable because they can act as stress concentration factors and, consequently, they can decrease part strength. The lack of visible delamination on the struts indicates that the process of bonding individual layers during the SLM process was correct.

3.2. Dimensional accuracy. The measurement from a CT scanner was used for geometric inspections and shape analyses. In the GOM Inspect software (GOM, Braunschweig, Germany), the real cellular lattice model, reconstructed from CT images, was superimposed onto the cellular lattice CAD model. After alignment, every point of the cellular lattice surface was compared with CAD reference data. The result of the comparison was a color-coded deviation map (Fig. 7, 8). The color deviation scales for the resultant maps were adjusted to fit the same range. The graph on the scale-bar shows the distribution of the deviations for the surface under consideration.

When analyzing the results, it can be seen that in some areas of the surface the maximum deviations are up to +0.25 (red color on the scale-bar). Referring the results obtained to the SEM observation, it can be concluded that the largest deviations were recorded in the places where spherical CP-Ti powders or partially melted agglomerates were attached to the struts surfaces. For other areas, average deviations for the cellular lattice structures being considered are within the range of +0.16/−0.08 mm. Yet another approach to the quantitative description of characteristic features of the struts was proposed by the authors in earlier work [29].

The micro-tomographic measurements allowed also to inspect whether there are defects (e.g. in the form of closed pores or layer delamination) in the solid part of the samples. From the mechanical properties point of view, they could be undesirable because these defects could reduce mechanical

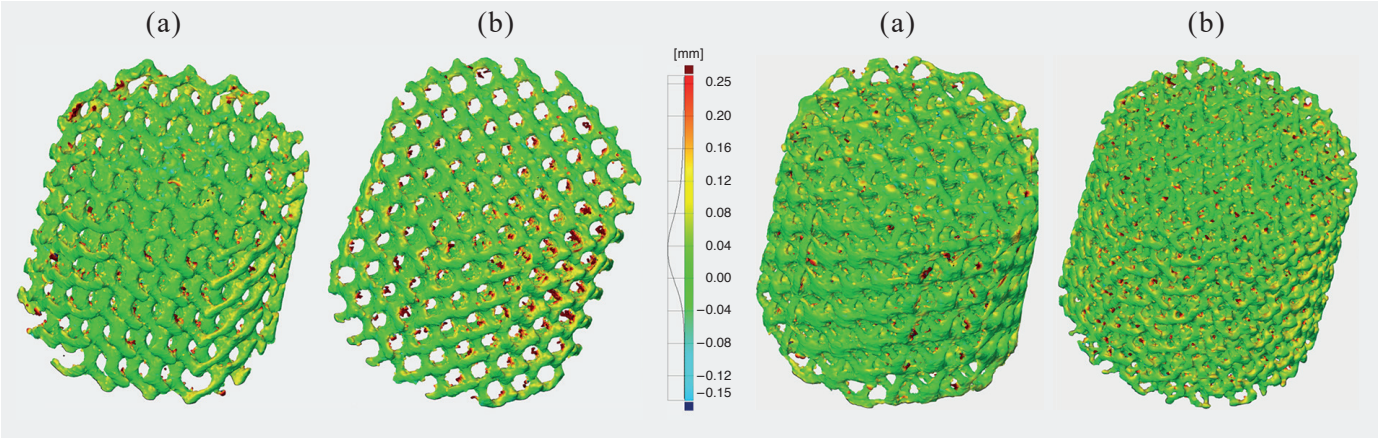

Fig. 7. Dimensional accuracy of: a) Gyr_6080, b) Diam_6080

Fig. 8. Dimensional accuracy of: a) IWP_6080, b) I2Y_6080

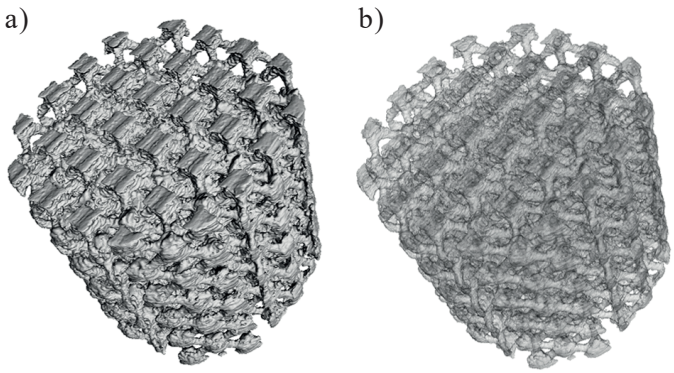

Fig. 9. 3D image obtained from: a) X-ray micro-tomography of the IWP_80 cellular lattice, b) visual inspection of the internal structure

properties. However, visual and quantitative inspection of the 3D volume (Fig. 9) did not show any pores or other defects in the solid part of the samples.

The porosity gradient was correctly reproduced in the entire volume of the sample. This is illustrated by the cross-sections in the Z axis shown in Fig. 10.

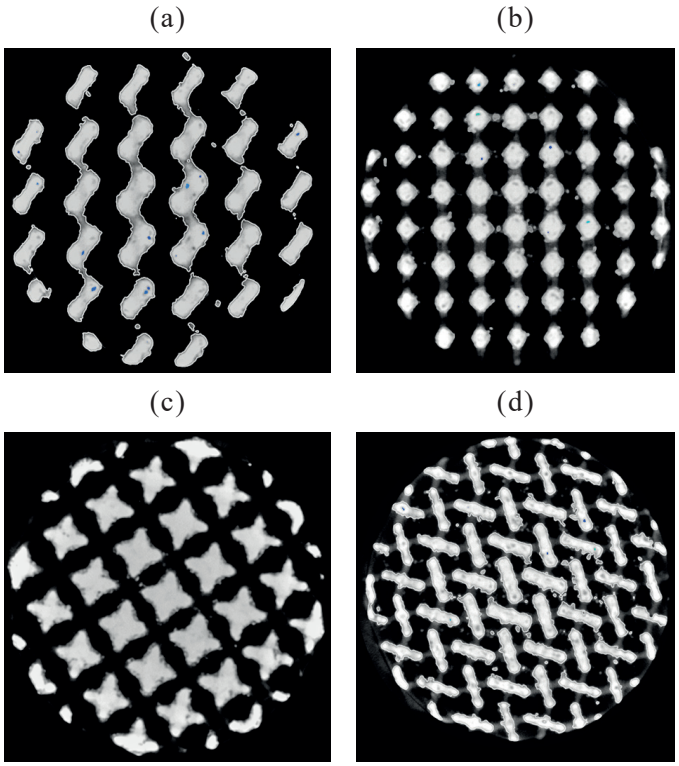

Fig. 10. Cross-sections relative to the xy plane for the a) Gyr, b) Diam, c) IWP, d) I2Y, cellular lattice with gradient porosity (X-ray micro-tomography)

When comparing the actual porosity of the samples, estimated by means of micro-tomography, and the nominal porosity resulting from model, it can be concluded that on average the total porosity of the manufactured samples is lower by 4% in relation to the porosity of the CAD model (Table 1, 3). However, the development of the surface increases significantly, which is related to partially melted particles, and which can be clearly seen in the scanning of electron microscope (SEM) micrographs.

Table 3
Basic parameters of the real cellular lattice

	S [cm^2]	V [cm^3]	V_v [%]	S/V [cm^2/cm^3]
Diam80	41.4	0.61	75.3	67.9
Gyr80	32.5	0.53	78.6	61.3
IWP80	37.4	0.60	75.7	62.4
I2Y80	54.5	0.55	77.8	99.0
Diam6080	40.9	0.71	71.3	57.7
Gyr6080	32.9	0.67	72.9	49.0
IWP6080	38.7	0.70	71.7	55.3
I2Y6080	66.8	0.84	66.0	79.5

where: S – surface area, V – volume of the model,
V_v – total porosity of the model, S/V – surface area to volume ratio

3.3. Mechanical properties. The behavior of metal foams in the uniaxial compression process is one of the most important features determining their usefulness as a construction material. In Fig. 12, stress strain curves recorded during uniaxial compression of cellular structures are presented. The stress-strain curves for the Gyr, IWP and I2Y samples are smooth and exhibit three characteristic regions: linear elasticity, plateau region and densification region (Fig. 11). With small strains, linear-elastic behavior is observed, with an inclination equal to the Young's modulus of the cellular lattice structure. As the load increases, the cells begin to deform plastically. The process proceeds under an approximately constant load, giving the pla-

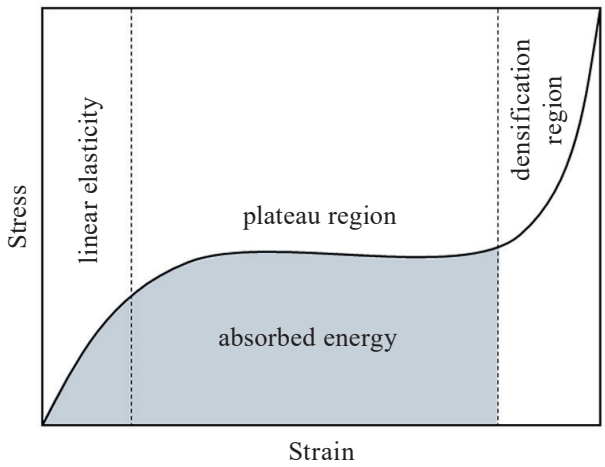

Fig. 11. Schematic presentation of the stress-strain curve for cellular lattice structure

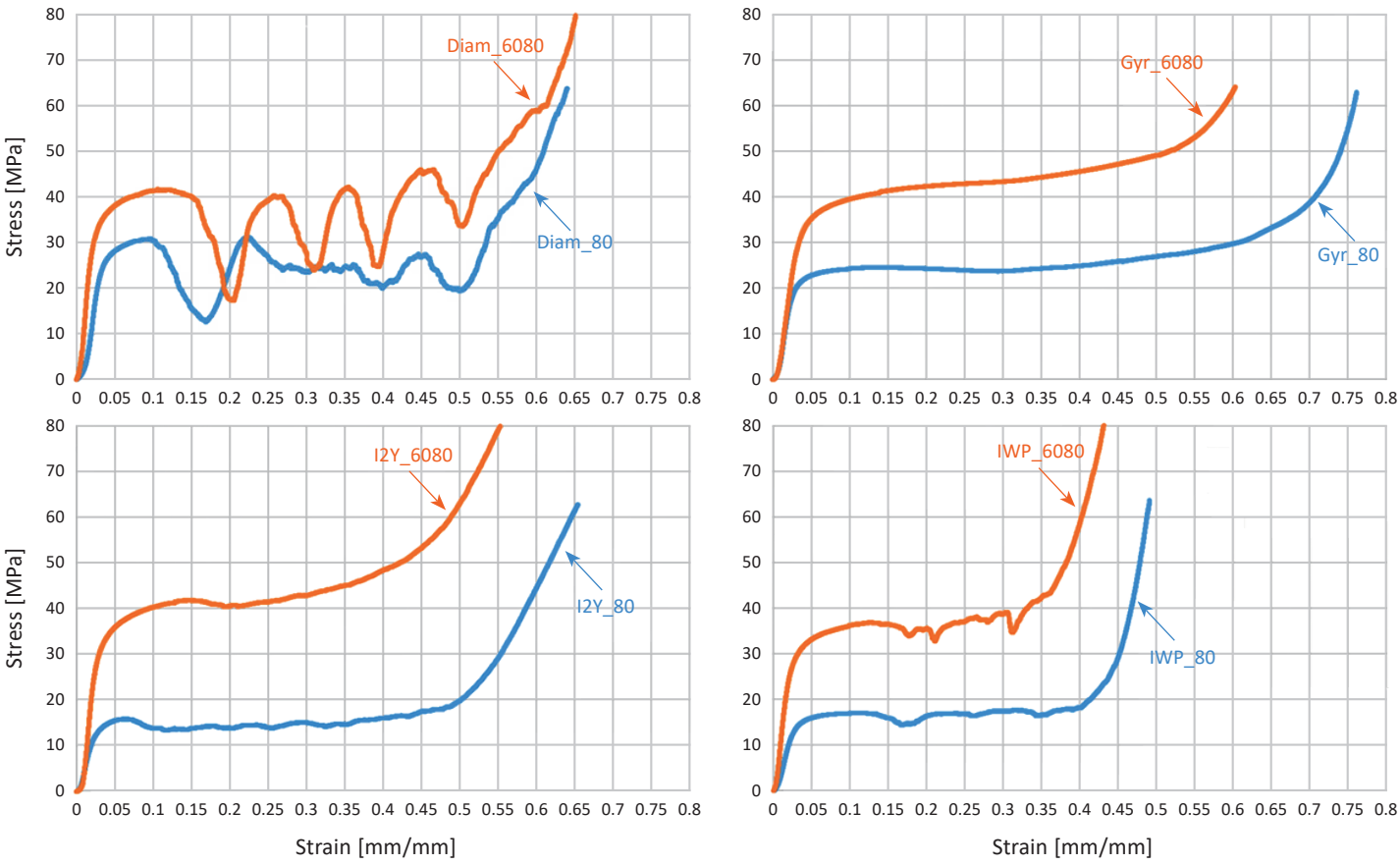

Fig. 12. Stress-strain curves for Diam, Gyr, I2Y and IWP cellular lattices

teau a stress. When the opposite walls of the cell of the cellular structure begin to touch, the densification process begins, resulting in a sharp increase in stress. The area under the curve from the initial stage to the beginning of densification represents the energy absorbed by the sample under fairly constant stress. The values of the plateau stress, densification strain and absorbed energy are all presented in Table 4.

Table 4
Mechanical properties of samples

	Plateau stress [MPa]	Densification strain [mm/mm]	Absorbed energy [J]
Diam80	23.5	0.50	33.4
Gyr80	25.5	0.70	46.3
IWP80	16.4	0.43	17.8
I2Y80	15.0	0.50	18.6
Diam6080	33.0	0.50	48.8
Gyr6080	43.2	0.56	59.5
IWP6080	36.0	0.35	31.6
I2Y6080	42.8	0.45	45.3

The shape of the plateau region for samples Diam_80 and Diam_6080 is different when compared to the other samples. The fluctuations in the stress value are clearly visible. This may indicate a rapid mechanism of destroying the cellular lattice struts with the increasing load. Keeping this fact in mind, just for this sample, the value of compressive strength was determined as the quotient of the maximum compressive force (first peak on the curve) and the area of the initial cross-section of the sample. The value was, respectively, 30.5 MPa and 41.5 MPa for sample Diam_80 and Diam_6080.

The stress-strain curve registered for Gyr-type samples has the smoothest shape. Moreover, these samples show a good cushioning effect because a nearly constant compression stress in the plateau region was registered for them. These samples were characterized also by the highest value of plateau stress and the energy absorbed, respectively: 25.5 and 43.2 MPa, 46.3 J and 59.5 J for Gyr_80 and Gyr_6080, which corresponds to a strain of almost 65% and 50%. This can positively affect the applicability of cellular structures with such topology.

In accordance with the initial assumption, samples with a porosity gradient were characterized by higher plateau stress as compared to the samples without gradient. The largest increase in the plateau stress value was recorded for the I2Y series, and it stood at 27.8 MPa (increase by 185%). The smallest increase was recorded for the G series, and it stood at 17.7 MPa (increase by 69%).

The cell structure geometry and gradient porosity significantly affect the strain value at which the cellular structure begins to densify. In this case, the smallest values were recorded for the IWP series at, respectively, 0.43 and 0.35 for sample IWP_80 and IWP_6080.

4. Conclusions

The presented modelling method allows for obtaining structures with smooth gradient transition of porosity for different elementary cell geometries. Selected parameters of the SLM process allowed to obtain samples with dense struts. No porosity was detected inside the solid beam. Both visual and quantitative comparisons indicated high accuracy of the SLM-built cellular lattice with and without gradient porosity. The difference in total porosity was on average 2–10%. The surface morphology of cellular lattice struts is very complicated. On the one hand, it may be appropriate because the roughness of the titanium surface affects the process and rate of osseointegration. On the other hand, such surface characteristics may act as stress concentrators and may lower mechanical properties of the cellular lattice structure, especially the fatigue strength [30]. It is also possible that weakly-attached particles will become detached from the surface. Therefore in the next study an additional surface modification treatment [31] and a different procedure to measure surface roughness will be considered [22, 32]. The behavior of the samples during uniaxial compression depends not only on the porosity, but also on the topology of the cellular lattice. As per the assumption, the core with lower porosity caused an increase in mechanical properties of the cellular lattice samples. The plateau stress increase ranged from 69% for the Gyr series to 185% for the I2Y series. The strain value at which the cellular structure begins to densify has the smallest value for the IWP series and the largest one for the Gyr series. The smoothest stress-strain curve observed for the Gyr series and good mechanical properties allows to comment positively on the applicability of cellular structures with such geometry. The results obtained will serve as the basis for future research, which will focus on the development of FEA models to predict the compressive response of lattice structures with radial gradient TPMS architecture.

Acknowledgements. This work was created as part of the research project No. DEC-2017/01/X/ST8/00780 funded by the National Science Centre, Poland. X-ray micro-tomography measurements were partially funded with a grant for education allocated by the Ministry of Science and Higher Education in Poland No. 02/22/DSPB/1432. This research was supported in part by PLGrid Infrastructure.

References

[1] B. Zhao, A.K. Gain, W. Ding, L. Zhang, X. Li, and Y. Fu, "A review on metallic porous materials: pore formation, mechanical properties, and their applications", *The International Journal of Advanced Manufacturing Technology*, 95(5–8), 2641–2659 (2018).

[2] F. García-Moreno, "Commercial applications of metal foams: Their properties and production", *Materials*, 9(2), 85 (2016).

[3] X.H. Han, Q. Wang, Y.G. Park, C. T'Joen, A. Sommers, and A. Jacobi, "A review of metal foam and metal matrix composites for heat exchangers and heat sinks", *Heat Transfer Engineering*, 33(12), 991–1009 (2012).

[4] P. Chabera, A. Boczkowska, A. Witek, and A. Oziębło, „Fabrication and characterization of composite materials based on porous ceramic preform infiltrated by elastomer", *Bull. Pol. Ac.: Tech.*, 63(1), 193–199 (2015).

[5] X.P. Tan, Y.J. Tan, C.S.L. Chow, S.B. Tor, and W.Y. Yeong, "Metallic powder-bed based 3D printing of cellular scaffolds for orthopaedic implants: A state-of-the-art review on manufacturing, topological design, mechanical properties and biocompatibility", *Materials Science and Engineering*: C, 76, 1328–1343 (2017).

[6] L.E. Murr, S.M. Gaytan, F. Medina, H. Lopez, E. Martinez, B.I. Machado, D.H. Hernandez, L. Martinez, M.I. Lopez, and R.B. Wicker, "Next-generation biomedical implants using additive manufacturing of complex, cellular and functional mesh arrays", *Philosophical Transactions of the Royal Society of London A: Mathematical, Physical and Engineering Sciences*, 368 (1917), 1999–2032 (2010).

[7] K. Pałka and R. Pokrowiecki, "Porous Titanium Implants: A Review", *Advanced Engineering Materials*, 20(5), 1700648, (2018).

[8] S.J. Hollister, "Scaffold design and manufacturing: from concept to clinic", *Advanced materials*, 21 (32–33), 3330–3342 (2009).

[9] S. Arabnejad, R.B. Johnston, J.A. Pura, B. Singh, M. Tanzer, and D. Pasini, "High-strength porous biomaterials for bone replacement: A strategy to assess the interplay between cell morphology, mechanical properties, bone ingrowth and manufacturing constraints", *Acta biomaterialia*, 30, 345–356 (2016).

[10] S.J. Hollister, R.D. Maddox, and J.M. Taboas, "Optimal design and fabrication of scaffolds to mimic tissue properties and satisfy biological constraints", *Biomaterials* 23(20), 4095–4103 (2002).

[11] N. Taniguchi, S. Fujibayashi, M. Takemoto, K. Sasaki, B. Otsuki, T. Nakamura, T. Matsushita, T. Kokubo, and S. Matsuda, "Effect of pore size on bone ingrowth into porous titanium implants fabricated by additive manufacturing: an in vivo experiment", *Materials Science and Engineering: C*, 59, 690–701 (2016).

[12] K. Kapat, P.K. Srivas, A.P. Rameshbabu, P.P. Maity, S. Jana, J. Dutta, P. Majumdar, D. Chakrabarti, and S. Dhara, "Influence of Porosity and Pore-Size Distribution in Ti6Al4 V Foam on Physicomechanical Properties, Osteogenesis, and Quantitative Validation of Bone Ingrowth by Micro-Computed Tomography", *ACS applied materials & interfaces*, 9(45), 39235–39248 (2017).

[13] F.M. Klenke, Y. Liu, H. Yuan, E.B. Hunziker, K.A. Siebenrock, and W. Hofstetter, "Impact of pore size on the vascularization and osseointegration of ceramic bone substitutes in vivo", *Journal of Biomedical Materials Research Part A: An Official Journal of The Society for Biomaterials, The Japanese Society for Biomaterials, and The Australian Society for Biomaterials and the Korean Society for Biomaterials*, 85(3), 777–786 (2008).

[14] W.J. Sames, F.A. List, S. Pannala, R.R. Dehoff, and S.S. Babu, "The metallurgy and processing science of metal additive manufacturing", *International Materials Reviews*, 61(5), 315–360 (2016).

[15] T.D. Ngo, A. Kashani, G. Imbalzano, K.T. Nguyen, and D. Hui, "Additive manufacturing (3D printing): A review of materials, methods, applications and challenges", *Composites Part B: Engineering*, 143 (15), 172–196 (2018).

[16] N. Chantarapanich, P. Puttawibul, S. Sucharitpwatskul, P. Jeamwatthanachai, S. Inglam, and K. Sitthiseripratip, "Scaffold library for tissue engineering: a geometric evaluation", *Computational and mathematical methods in medicine*, (2012).

[17] M. Fantini, M. Curto, and F. De Crescenzio, "A method to design biomimetic scaffolds for bone tissue engineering based on Voronoi lattices", *Virtual and Physical Prototyping*, 11(2), 77–90 (2016).

[18] C.M. Cheah, C.K. Chua, K.F. Leong, C.H. Cheong, and M.W. Naing, "Automatic algorithm for generating complex polyhedral scaffold structures for tissue engineering", *Tissue Engineering*, 10(3–4), 595–610 (2004).

[19] J. Shi, L. Zhu, L. Li, Z. Li, J. Yang, and X. Wang, "A TPMS-based method for modeling porous scaffolds for bionic bone tissue engineering", *Scientific reports*, 8(1), 7395 (2018).

[20] D.J. Yoo, "Computer-aided porous scaffold design for tissue engineering using triply periodic minimal surfaces", *International Journal of Precision Engineering and Manufacturing*, 12(1), 61–71 (2011).

[21] D.J. Yoo, "Heterogeneous porous scaffold design for tissue engineering using triply periodic minimal surfaces", *International Journal of Precision Engineering and Manufacturing*, 13(4), 527–537 (2012).

[22] A. Thompson, N. Senin, C. Giusca, and R. Leach, "Topography of selectively laser melted surfaces: a comparison of different measurement methods", *CIRP Annals*, 66(1), 543–546 (2017).

[23] L. Yang, R. Mertens, M. Ferrucci, C. Yan, Y. Shi, and S. Yang "Continuous graded Gyroid cellular structures fabricated by selective laser melting: Design, manufacturing and mechanical properties", *Materials & Design*, 162, 394–404 (2019).

[24] S.L. Sing, W.Y. Yeong, F.E. Wiria, and B.Y. Tay, "Characterization of titanium lattice structures fabricated by selective laser melting using an adapted compressive test method", *Experimental Mechanics*, 56(5), 735–748, (2016).

[25] B. Gapinski, M. Wieczorowski, L. Marciniak-Podsadna, B. Dybala, and G. Ziolkowski, "Comparison of Different Methods of Measurement Geometry Using CMM, Optical Scanner and Computed Tomography 3D", *Procedia Engineering*, 69, 255–262 (2014).

[26] B. Gapiński, M. Wieczorowski, M. Grzelka, P. Arroyo Alonso, and A. Bermúdez Tomé, "The application of micro CT to assess quality of workpieces manufactured by means of rapid prototyping", *Polimery*, 1, 53–59 (2017).

[27] J.P. Kruth, M. Bartscher, S. Carmignato, R. Schmitt, L. De Chiffre, and A. Weckenmann, "Computed tomography for dimensional metrology", *CIRP Annals-Manufacturing Technology*, 60(2), 821–842 (2011).

[28] X. Han, H. Zhu, X. Nie, G. Wang, and X. Zeng, "Investigation on selective laser melting AlSi10Mg cellular lattice strut: molten pool morphology, surface roughness and dimensional accuracy", *Materials*, 11(3), 392 (2018).

[29] J. Maszybrocka, A. Stwora, B. Gapiński, G. Skrabalak, and M. Karolus, "Morphology and surface topography of Ti6Al4V lattice structure fabricated by selective laser sintering", *Bull. Pol. Ac.: Tech.*, 65(1), 85–92 (2017).

[30] M. Dallago, V. Fontanari, E. Torresani, M. Leoni, C. Pederzolli, C. Potrich, and M. Benedetti, "Fatigue and biological properties of Ti-6Al-4V ELI cellular structures with variously arranged cubic cells made by selective laser melting", *Journal of the mechanical behavior of biomedical materials*, 78, 381–394 (2018).

[31] S.M. Ahmadi, R. Kumar, E.V. Borisov, R. Petrov, S. Leeflang, Y. Li, and V.A. Popovich, "From microstructural design to surface engineering: A tailored approach for improving fatigue life of additively manufactured meta-biomaterials", *Acta biomaterialia*, 83, 153–166 (2019).

[32] J. Józwik, D. Ostrowski, R. Milczarczyk, and G.M. Krolczyk, „Analysis of relation between the 3D printer laser beam power and the surface morphology properties in Ti-6Al-4V titanium alloy parts" *Journal of the Brazilian Society of Mechanical Sciences and Engineering*, 40(4), 215 (2018).